NANO LETTERS

Open Access
This article is licensed under CC-BY 4.0

pubs.acs.org/NanoLett
Letter

Stacking-Order-Dependent Electronic Properties of $MoTe_2/WSe_2$ Moiré Bilayers

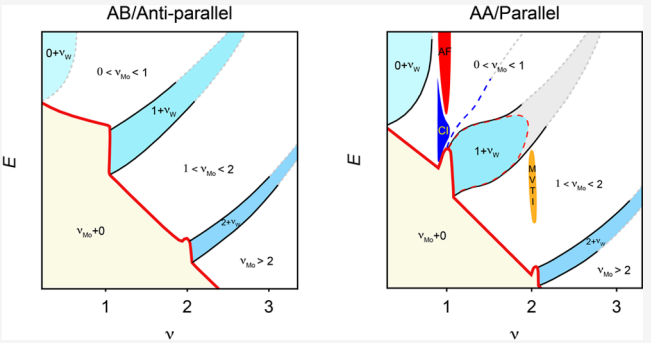
Zhongdong Han, Wenjin Zhao, Eegene Clara Chung, Chia-Hao Lee, Zui Tao, Zhengchao Xia, Yichi Zhang, Yiyu Xia, Jekwan Lee, Bowen Shen, Ariana Ray, Yu-Tsun Shao, Tingxin Li, Shengwei Jiang, Yihang Zeng, Kenji Watanabe, Takashi Taniguchi, David A. Muller, Kin Fai Mak,* and Jie Shan*

Cite This: *Nano Lett.* 2026, 26, 14829−14836

Read Online

ACCESS | Metrics & More | Article Recommendations | Supporting Information

ABSTRACT: Transition metal dichalcogenide (TMD) moiré bilayers have realized a wide range of strongly correlated and topological phenomena. The physics in these materials is often sensitive to the interlayer stacking order. Polarization-resolved optical second harmonic generation (SHG) is the most used technique for stacking order characterization but unverified for most heterobilayers. Here we calibrate the optical SHG for angle-aligned $MoTe_2/WSe_2$ bilayers by the scanning transmission electron microscopy (STEM). We directly compare the transport and magnetic properties and the electronic phase diagram for two distinct stacking orders. With the calibrated stacking order assignment, we clarify the interpretation of earlier results, including the nature of the Chern insulator, mechanism of an electric-field-tuned metal−insulator transition at half band filling, and the Kondo lattice physics. Our work provides a consistent picture of the relation between the stacking order and the electronic properties of $MoTe_2/WSe_2$ moiré bilayers.



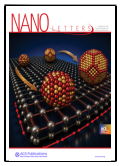
KEYWORDS: *TMD moiré bilayers, stacking order, electronic properties, SHG, STEM, interlayer hybridization*

Semiconductor moiré materials have emerged as a highly tunable platform for studying electronic correlations and topology. A wide range of phenomena, including Mott and Wigner-Mott insulators,[1−14] kinetic antiferromagnetism and spin polarons,[15−19] Kondo lattice physics,[20−28] and the quantum anomalous Hall[29−36] and quantum spin Hall effects,[29,34,37,38] has been demonstrated in one system--angle-aligned $MoTe_2/WSe_2$ vertical heterobilayers.[39−42] Many of these phenomena are sensitive to stacking order, that is, whether the two transition metal dichalcogenide (TMD) monolayers are parallel (AA-stacking) or antiparallel (AB-stacking) to each other (Figure 1a,b).

Angle-aligned $MoTe_2/WSe_2$ bilayers form a moiré lattice with period $a_M \approx 5$ nm because of the 7% lattice mismatch between the two TMDs. The electronic states of interest are originated from the valence band in the K/K′ valley of monolayer $MoTe_2$ or WSe_2, where the presence of a strong Ising spin−orbit interaction creates a large spin splitting in each valley and the spin and valley degrees of freedom are locked.[41,43] Because the moiré momentum is negligible compared to the atomic scale momentum, moiré bands can hybridize only with those from the same valley (Figure 1c). The spin-valley locking renders the moiré band structure stacking dependent: interlayer hybridization is spin allowed for AA-stacking and spin forbidden for AB-stacking.[31] This stacking-dependent interlayer hybridization, however, poses significant challenges in understanding several earlier experimental results, including the nature of the Chern insulator, mechanism of an electric-field-tuned metal−insulator transition at half band filling, and the Kondo lattice physics.[1,20,29,37]

In all previous experiments, stacking order in angle-aligned $MoTe_2/WSe_2$ bilayers was determined by the polarization-resolved optical second harmonic generation (SHG).[44,45] Specifically, monolayer TMDs lacking inversion symmetry allow for a second-order response; the second harmonic (SH) dipole moment is uniquely determined by the crystal's symmetry.[46−48] In angle-aligned bilayers, the SH dipole from each monolayer is expected to be in-phase (out-of-phase) for AA-(AB-)stacking, leading to constructive (destructive) interference of the SH radiation. This convenient optical technique has been extensively studied in natural TMD bilayers and multilayers[46−48] but remained unverified for

Received: May 20, 2026
Revised: October 15, 2026
Accepted: October 20, 2026
Published: October 26, 2026



ACS Publications
© 2026 The Authors. Published by American Chemical Society

https://doi.org/10.1021/acs.nanolett.6c02425
Nano Lett. 2026, 26, 14829−14836

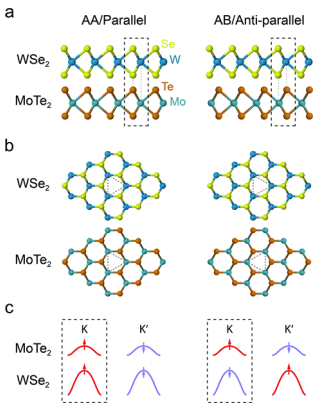


Figure 1. Stacking order and moiré bands of angle-aligned $MoTe_2/WSe_2$ bilayers. a, Side view. b, Top view. The atoms are shown in blue (W), green (Se), cyan (Mo) and brown (Te). c, Spin-resolved topmost moiré valence bands from $MoTe_2$ and WSe_2. Left: AA-stacking with two layers parallel to each other; right: AB-stacking with two layers antiparallel to each other. In each valley (K/K′), electron spins (arrows) in the two layers are parallel (AA) or antiparallel (AB) due to spin-valley locking in monolayer TMDs. Interlayer hybridization is spin allowed for AA-stacking and spin forbidden for AB-stacking.

heterobilayers except WS_2/WSe_2 (refs 44 and 45). In this work, we directly determine the stacking order in angle-aligned $MoTe_2/WSe_2$ bilayers by the scanning transmission electron microscopy (STEM) and establish a correlation between the stacking order and SHG. Contrary to homobilayers, we observe destructive interference in SHG for AA-stacked $MoTe_2/WSe_2$ bilayers with excitation at 800 nm. Based on the revised stacking order assignment, we present a consistent picture of stacking-dependent electronic phase diagrams of the material.

STRUCTURE CHARACTERIZATION

We directly determine the structure of $MoTe_2/WSe_2$ bilayers by atomic-resolution imaging using STEM. The annular dark-field (ADF) image intensity scales approximately with $Z^{1.7}$, where Z is the atomic number (ref.[49]), and the contributions from overlapping chalcogen atoms are summed (Table 1). The

Table 1. ADF-STEM Intensity Scaling with Atomic Numbers in $MoTe_2/WSe_2$ Bilayers[a]

element	atomic number Z	HAADF contrast $\sim Z^{1.7}$	total contrast (a.u.)
Mo	42	575	575
W	74	1505	1505
Se	34	401	802 (Se_2)
Te	52	826	1652 (Te_2)

[a]The high-angle annular dark-field (HAADF) contrast is approximately proportional to $Z^{1.7}$ (ref 49). The contributions from overlapping chalcogen atoms are summed (a.u.: arbitrary unit).

atoms in each TMD monolayer can be clearly identified: the W sites appear about two times brighter than the Se_2 sites in WSe_2, and the Te_2 sites are about three times brighter than the Mo sites in $MoTe_2$. But the W and Te_2 sites have similar intensities, making accurate identification of the atoms and consequently stacking order in heterobilayers difficult.

We designed a special sample geometry to unambiguously determine the stacking order in $MoTe_2/WSe_2$ bilayers by STEM and correlate it with SHG (see Methods for details on the sample fabrication and STEM and SHG measurements). Figure 2a,b shows two $MoTe_2/WSe_2$ samples angle aligned

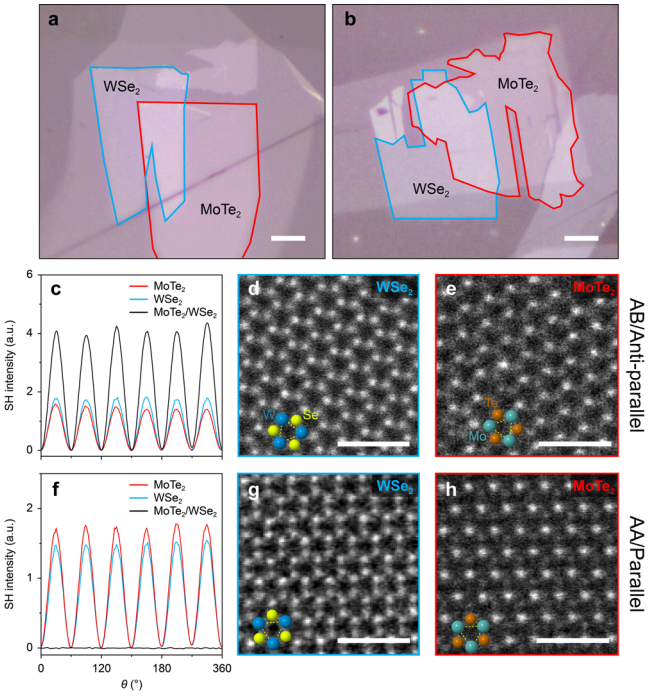


Figure 2. Stacking order determination. a, b, Optical images of angle-aligned $MoTe_2/WSe_2$ sample 1 (a) and sample 2 (b) on PC stamps. The WSe_2 and $MoTe_2$ layers are outlined in blue and red, respectively. Scale bars are 5 μm. The WSe_2 ($MoTe_2$) layers were cut from the same flake. A 180° rotation was introduced in the two $MoTe_2$ layers. SHG with excitation at 800 nm and STEM measurements were performed on both the isolated monolayer regions and the bilayer region (Methods). c–e, Characterization of sample 1. The SH intensity (c) exhibits a 6-fold rotational symmetry as a function of the excitation polarization angle. The bilayer response is 2–3 times of that of each monolayer. ADF-STEM images from the WSe_2 (d) and $MoTe_2$ (e) monolayer regions identify the atoms (colored balls) and the metal sublattices (marked by yellow dashed lines). Scale bars are 1 nm. f–h, Characterization for sample 2. The SH intensity for the bilayer nearly vanishes.

based on SHG. The $MoTe_2$ and WSe_2 monolayers in these samples were cut from the same flakes and one $MoTe_2$ layer was rotated by 180° relative to the other. The two bilayer samples are thus guaranteed to have different stacking orders. Figure 2d,e shows the ADF-STEM images of the isolated WSe_2 and $MoTe_2$ monolayer regions of sample 1 (Figure 2a). Intensity profile analysis of these images (Figure S1) clearly identifies the metal and chalcogen atoms. We determine the overlapped region to be AB-stacked based on the relative orientations of the metal sublattices (denoted by yellow dashed lines) in the isolated monolayer regions. Similarly, we determine sample 2 (Figure 2b) to be AA-stacked based on the ADF-STEM images in Figure 2g,h (see Figure S2,3 for STEM images of the bilayer regions for further confirmation of the stacking order assignment).

We correlate the SHG with stacking order by performing SH measurements on both the isolated monolayer regions and the bilayer region (Figure 2c,f). We used the reflection geometry with normal incidence for excitation at 800 nm. The SH intensity in cross-polarization exhibits a 6-fold symmetric

https://doi.org/10.1021/acs.nanolett.6c02425
Nano Lett. 2026, 26, 14829–14836

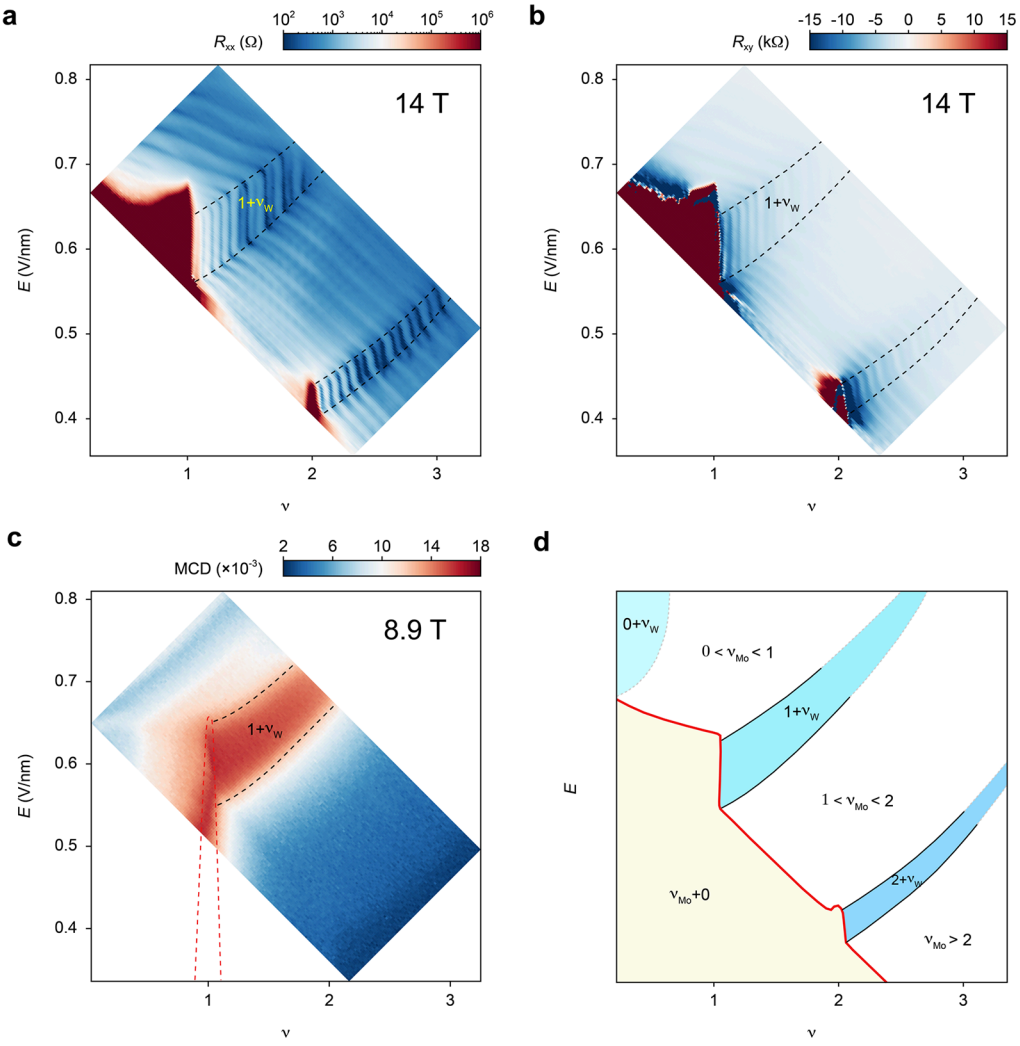


Figure 3. Electronic phase diagram for an AB-stacked device. Data are obtained from a device whose stacking structure is characterized by SHG only. a, b, Longitudinal resistance R_{xx} (a) and Hall resistance R_{xy} (b) as a function of ν and E at T = 1.6 K and B = 14 T. Regions $(1 + \nu_W)$ and $(2 + \nu_W)$ (enclosed by dashed lines) exhibit vertical stripes. c, MCD as a function of ν and E at T = 1.6 K and B = 8.9 T. The Mott insulating state at $\nu_{Mo} = 1$ and region $(1 + \nu_W)$ show a large MCD response and are marked by red and black dashed lines, respectively. d, Schematic phase diagram. Regions are labeled by filling factors in the WSe_2 and $MoTe_2$ layers.

response as a function of the linear polarization angle of the excitation beam, or equivalently, the crystal's azimuthal angle. Such a response is consistent with the 3-fold rotational symmetry of monolayer TMDs[46−48] and agrees with previous reports.[1,29] The SH intensity is comparable for monolayer $MoTe_2$ and WSe_2. But surprisingly, it nearly vanishes for the AA-stacked sample (Figure 2f) and is about 2−3 times of that of each monolayer for the AB-stacked sample. The imperfect constructive interference in the latter is likely caused by the finite optical absorption at the SH wavelength (400 nm) and by stacking-induced modifications on the optical response.

The result highlights that the SH response is a frequency-dependent complex function and can be significantly altered when either the fundamental or SH radiation is close to an electronic transition. Given the large difference in two TMDs' band gaps and the 800 nm excitation lying between the two gap values, a phase shift between the SH dipole moments from two layers in AA-stacked bilayers is generally expected. This is further supported by the excitation wavelength dependence of SHG from another AA-stacked $MoTe_2/WSe_2$ bilayer (Figure S4). We observe destructive interference of the SH radiation for all three excitation wavelengths (800 nm, 1100 and 1220 nm), with most complete cancelation at 800 nm. The results are fully consistent with a recent detailed wavelength-dependence study on the same material.[50] The *ab initio* calculations in ref.[50] further suggest a π-phase shift in the SH response of the two TMD layers due to their distinct two-photon resonances.

■ ELECTRONIC PHASE DIAGRAMS

Equipped with the calibrated SHG, we study the correlation between the stacking order and the electronic phase diagram in dual-gated $MoTe_2/WSe_2$ devices (whose stacking orders were characterized by SHG only) by combining the electrical transport and magnetic circular dichroism (MCD) measurements. The latter characterizes the magnetic properties of the bilayers. (See Methods and Figure S5 for stacking-order-dependent exciton hybridization). The two gates allow independent control of the lattice filling factor (ν) of holes in the bilayer and the electric field (E) perpendicular to the sample plane. Compared to earlier works, we used thinner hexagonal boron nitride (hBN) gate dielectrics to access higher

https://doi.org/10.1021/acs.nanolett.6c02425
Nano Lett. 2026, 26, 14829−14836

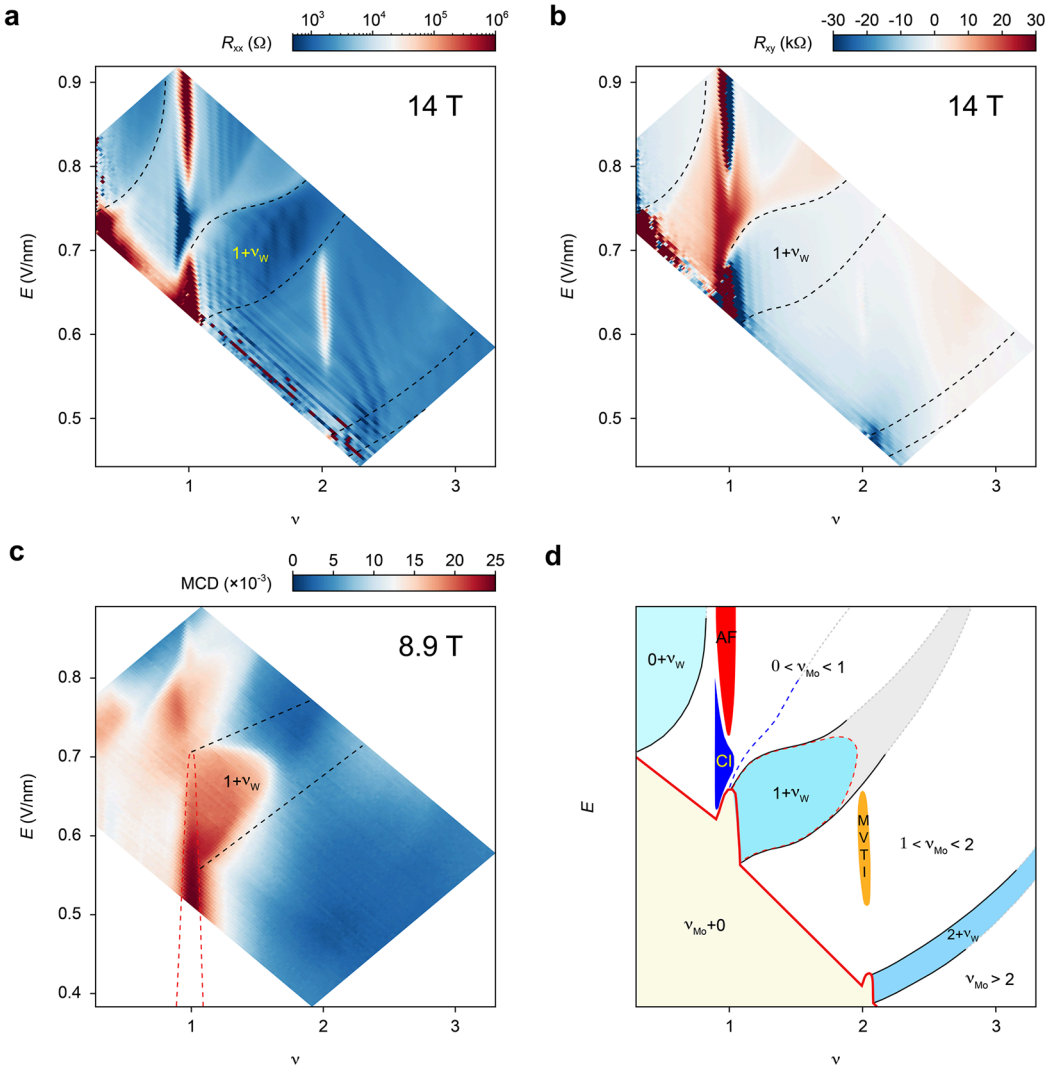


Figure 4. Electronic phase diagram for an AA-stacked device. Data are obtained from a device whose stacking structure is characterized by SHG only. Same as Figure 3 for an AA-stacked $MoTe_2/WSe_2$ bilayer. New states emerge in the phase diagram (d), including a Chern insulator (CI)[29] and an antiferromagnetic (AF) insulator[68] at $\nu = 1$ and a mixed-valence topological insulator (MVTI)[22] at $\nu = 2$. The blue dashed line in region ($0 < \nu_{Mo} < 1$) separates two Fermi surfaces: one with $R_{xy} > 0$ and another with $R_{xy} < 0$ and vertical SdH stripes; the latter has a small Fermi surface with doping counted from $\nu = 1$. The red dashed line within region ($1 + \nu_W$) separates a light (blue-shaded) and heavy (gray-shaded) Fermi liquid. The former shows strong MCD.

breakdown fields and wider phase diagrams.[22] Unless otherwise specified, the sample temperature was 1.6 K. See Methods for details on device fabrication and electrical and magneto-optical measurements.

The results for an AB-stacked $MoTe_2/WSe_2$ bilayer are shown in Figure 3. Figure 3a,b shows the longitudinal (R_{xx}) and Hall (R_{xy}) resistances, respectively, as a function of ν and E under a perpendicular magnetic field $B = 14$ T. The resistance maps are dominated by stripes, originating from the Shubnikov-de Haas (SdH) oscillations in the WSe_2 layer, which has a more dispersive moiré valence band and higher hole mobility. (Substantially weaker SdH oscillations in the $MoTe_2$ layer can also be discerned especially in the region of $1 < \nu < 2$). Diagonal stripes show that both layers are charge compressible and the partition in doping is tunable by electric field. In contrast, vertical stripes show that the $MoTe_2$ layer is incompressible and the hole density in the WSe_2 layer is independent of electric field.

We construct the electrostatic phase diagram in Figure 3d from the transport data. In the yellow region ($\nu_{Mo} + 0$, left to the red solid line), only the $MoTe_2$ layer is doped and the WSe_2 layer is charge neutral ($MoTe_2/WSe_2$ is a type I heterojunction at $E = 0$ with the $MoTe_2$ band gap lying entirely inside the WSe_2 band gap). Here ν_{Mo} and ν_W denote the hole filling factors of the $MoTe_2$ and WSe_2 layers, respectively. The resistance in this region is generally high, likely due to the flat $MoTe_2$ Hubbard bands, which favor charge localization. The other limit is the high E-field region ($0 + \nu_W$), where the WSe_2 layer is doped and the $MoTe_2$ layer is charge neutral. We could not access this region experimentally due to dielectric breakdown. In the two middle blue regions, the stripes are vertical, showing that the Fermi level is inside a gap of the $MoTe_2$ layer—a Mott gap for ($1 + \nu_W$) and a moiré band gap for ($2 + \nu_W$)—and only the WSe_2 layer hosts itinerant holes. The rest phase regions bear generic filling factors.

The constructed phase diagram is supported by the magnetic response of the bilayer. Figure 3c is the spectrally

https://doi.org/10.1021/acs.nanolett.6c02425
Nano Lett. 2026, 26, 14829−14836

averaged MCD over the attractive polaron resonance of $MoTe_2$ as a function of ν and E at B = 8.9 T. Strong MCD response is observed mainly around ν_{Mo} = 1 (denoted by red dashed lines) and in region (1 + ν_W, marked by black dashed lines). This is consistent with the $MoTe_2$ layer being a Mott insulator at half band filling; the spins after charge localization (i.e., local magnetic moments) are highly polarizable, giving a strong MCD response[44] relative to the other phase regions.

The corresponding results for an AA-stacked $MoTe_2/WSe_2$ bilayer are shown in Figure 4 (see Figure S6,7 for comparison of resistance and MCD at B = 0). They are consistent with previous reports.[20,29,37] The resistance maps (Figure 4a,b) share some similarities with those of the AB-stacked sample but are substantially richer. Similarly, we observe vertical resistance stripes in regions (0 + ν_W), (1 + ν_W) and (2 + ν_W), and field-dispersive stripes in region (1 < ν_{Mo} < 2). On the other hand, we find vertical instead of diagonal stripes in region (0 < ν_{Mo} < 1) and new insulating states at ν = 1 and ν = 2. Particularly, the insulating state at ν = 1 for the intermediate E-fields, exhibiting vanishing R_{xx} and quantized R_{xy}, is a Chern insulator (Figure 4d). In the presence of finite interlayer hybridization, the layer-resolved filling factors (ν_{Mo} and ν_W) become approximate.

The MCD map under B = 8.9 T (Figure 4c) also shows some similarities and differences between the two stacking orders. Specifically, a strong MCD response is also observed around ν_{Mo} = 1 and in region (1 + ν_W) for the AA-stacked sample, where the $MoTe_2$ layer is a Mott insulator. However, the strong MCD response in region (1 + ν_W) terminates at an arc-shaped boundary, which expands into higher fillings with increasing magnetic field,[51] whereas for the AB-stacked sample, strong MCD persists throughout the entire region. In addition, strong MCD is observed around ν = 1 for the intermediate E-fields, in accord with the Chern insulator.

The results in Figure 3,4 are consistent with the stacking dependent interlayer hybridization. The most important difference between the two stacking orders is how the SdH oscillations behave in regions with generic fillings. The AB-stacked samples have negligible interlayer hybridization. Therefore, the Landau levels in two layers are decoupled; both can be populated by gating and shifted in energy by electric field; the SdH stripes are diagonal in regions with generic fillings. Conversely, the AA-stacked samples have finite interlayer hybridization, weakening the electric-field effects. The Landau levels are layer hybridized in region (0 < ν_{Mo} < 1) and the stripes are field independent. The stripes show field dispersion in region (1 < ν_{Mo} < 2) but are still substantially different from the layer-decoupled case, indicating weaker but non-negligible interlayer hybridization. Furthermore, the mixed valence topological insulator (MVTI) exhibiting the quantum spin Hall effect at ν = 2 and the Chern insulator at ν = 1 (in the presence of strong Coulomb interactions[31−35,52,53]) require interlayer hybridization and are observed only in AA-stacked samples (Figure 4d).

REVISED INTERPRETATION OF EARLIER RESULTS

With a better understanding of the relationship between the stacking order and electronic phase diagram, we clarify the interpretation of several earlier studies. The first concerns the nature of the Chern insulator at ν = 1. An earlier study assigned the samples as AB-stacked bilayers based on the uncalibrated SHG.[29] By studying the layer-resolved MCD response, ref.[54] further concluded that the Chern state is valley coherent. Based on the corrected stacking order assignment and the reported layer-resolved MCD results,[54] we conclude that the Chern insulator is a valley-polarized state, which is consistent with most theoretical expectations.[31−35]

The second is the metal−insulator transition induced by electric field at fixed filling ν = 1 (ref 1). The transition was thought to occur in AA-stacked samples based on the uncalibrated SHG. The metal−insulator transition was interpreted as a bandwidth-tuned Mott transition because electric field in AA-stacked bilayers can tune the moiré bandwidth like in small-angle twisted homobilayers.[52,53,55−66] With the revised stacking order assignment, we note that moiré bandwidth tuning by electric field is unlikely due to the negligible interlayer hybridization in AB-stacked bilayers. But electric field can tune the charge transfer gap between the WSe_2 moiré band and the $MoTe_2$ Hubbard band through the linear interlayer Stark effect. The charge transfer gap, acting as a Mott gap, is continuously tuned to zero at the metal−insulator transition; such a transition belongs to the same universality class as the bandwidth-tuned Mott transition.[67]

The last concerns the Kondo lattice phenomena observed in region (1 + ν_W) of the phase diagram. The samples were assigned as AB-stacked bilayers based on the uncalibrated SHG previously,[20] but their negligible interlayer hybridization would imply a negligible Kondo coupling. The difficulty is resolved by the revised stacking order assignment: the finite interlayer hybridization in AA-stacked samples produces a measurable Kondo coupling between the local moments in the $MoTe_2$ layer and the itinerant holes in the WSe_2 layer. The arc-shaped boundary in the MCD response under a fixed B-field (Figure 4c) separates a light Fermi liquid and a heavy Fermi liquid as reported in ref.[51] To the left of the boundary, the Zeeman field overcomes the Kondo coupling, the local moments and the itinerant holes are decoupled, and the polarized local moments give a strong MCD response. To the right of the boundary, the local moments and the itinerant holes are coupled to form Kondo singlets, resulting in a weak MCD response. The shape of the boundary is given by the dependence of Kondo coupling on the filling factor and band alignment (or electric field). In contrast, the strong MCD or local moment response is observed throughout region (1 + ν_W) for AB-stacked bilayers (Figure 3c).

In summary, stacking order plays a crucial role in the electronic properties of TMD moiré bilayers because interlayer hybridization is stacking-order dependent. In this study, we calibrated the optical SHG—a commonly used technique for the stacking order characterization—by atomic resolution imaging using the STEM. Once the calibration is established, only SHG characterization is required to determine the stacking order of $MoTe_2/WSe_2$ moiré bilayers in future studies. We also directly correlate the stacking order with the transport and magnetic properties and the electronic phase diagram of the material. With the revised stacking order assignment, we resolved difficulties in the interpretation of earlier results, including the nature of the Chern insulator, mechanism of an electric-field-tuned metal−insulator transition at half band filling, and the Kondo lattice physics. Our work highlights the importance of calibrating SHG by STEM in determining the stacking orders of angle-aligned TMD heterobilayers in general; it also establishes an experimental approach for correlating SHG and STEM characterizations for generic air-sensitive layered heterostructures.

https://doi.org/10.1021/acs.nanolett.6c02425
Nano Lett. 2026, 26, 14829−14836

■ ASSOCIATED CONTENT

Supporting Information

The Supporting Information is available free of charge at https://pubs.acs.org/doi/10.1021/acs.nanolett.6c02425.

Methods for STEM and Hall bar device fabrication; STEM, SHG, electrical transport, and magneto-optical measurement procedures; stacking-dependent exciton hybridization; supplementary figures on atomic-resolution imaging, stacking-order determination, SHG wavelength dependence, exciton hybridization, and zero-field transport and MCD (PDF)

■ AUTHOR INFORMATION

Corresponding Authors

Kin Fai Mak − *Laboratory of Atomic and Solid State Physics, Department of Physics, and School of Applied and Engineering Physics, Cornell University, Ithaca, New York 14853, United States; Max Planck Institute for the Structure and Dynamics of Matter, Hamburg 22761, Germany; Kavli Institute at Cornell for Nanoscale Science, Ithaca, New York 14853, United States;* orcid.org/0000-0002-5768-199X; Email: kin-fai.mak@mpsd.mpg.de

Jie Shan − *Laboratory of Atomic and Solid State Physics, Department of Physics, and School of Applied and Engineering Physics, Cornell University, Ithaca, New York 14853, United States; Max Planck Institute for the Structure and Dynamics of Matter, Hamburg 22761, Germany; Kavli Institute at Cornell for Nanoscale Science, Ithaca, New York 14853, United States*; Email: jie.shan@mpsd.mpg.de

Authors

Zhongdong Han − *Laboratory of Atomic and Solid State Physics and Department of Physics, Cornell University, Ithaca, New York 14853, United States; Max Planck Institute for the Structure and Dynamics of Matter, Hamburg 22761, Germany;* orcid.org/0000-0003-3296-5563

Wenjin Zhao − *Kavli Institute at Cornell for Nanoscale Science, Ithaca, New York 14853, United States;* orcid.org/0000-0003-0016-5684

Eegene Clara Chung − *Department of Physics and School of Applied and Engineering Physics, Cornell University, Ithaca, New York 14853, United States;* orcid.org/0000-0002-6626-2746

Chia-Hao Lee − *School of Applied and Engineering Physics, Cornell University, Ithaca, New York 14853, United States*

Zui Tao − *School of Applied and Engineering Physics, Cornell University, Ithaca, New York 14853, United States*

Zhengchao Xia − *School of Applied and Engineering Physics, Cornell University, Ithaca, New York 14853, United States*

Yichi Zhang − *Department of Physics, Cornell University, Ithaca, New York 14853, United States*

Yiyu Xia − *School of Applied and Engineering Physics, Cornell University, Ithaca, New York 14853, United States*

Jekwan Lee − *Laboratory of Atomic and Solid State Physics and Department of Physics, Cornell University, Ithaca, New York 14853, United States; Max Planck Institute for the Structure and Dynamics of Matter, Hamburg 22761, Germany*

Bowen Shen − *School of Applied and Engineering Physics, Cornell University, Ithaca, New York 14853, United States*

Ariana Ray − *Department of Physics, Cornell University, Ithaca, New York 14853, United States;* orcid.org/0000-0002-9210-4880

Yu-Tsun Shao − *School of Applied and Engineering Physics, Cornell University, Ithaca, New York 14853, United States;* orcid.org/0000-0002-5574-0490

Tingxin Li − *School of Applied and Engineering Physics, Cornell University, Ithaca, New York 14853, United States*

Shengwei Jiang − *Laboratory of Atomic and Solid State Physics and Department of Physics, Cornell University, Ithaca, New York 14853, United States*

Yihang Zeng − *Laboratory of Atomic and Solid State Physics and Department of Physics, Cornell University, Ithaca, New York 14853, United States;* orcid.org/0000-0003-2941-5958

Kenji Watanabe − *National Institute for Materials Science, Tsukuba 305-0047, Japan;* orcid.org/0000-0003-3701-8119

Takashi Taniguchi − *National Institute for Materials Science, Tsukuba 305-0047, Japan;* orcid.org/0000-0002-1467-3105

David A. Muller − *Kavli Institute at Cornell for Nanoscale Science, Ithaca, New York 14853, United States; School of Applied and Engineering Physics, Cornell University, Ithaca, New York 14853, United States*

Complete contact information is available at: https://pubs.acs.org/10.1021/acs.nanolett.6c02425

Author Contributions

Z.H., W.Z., and Yichi Zhang fabricated the STEM samples. Z.H., Yichi Zhang, and Y.X. fabricated the transport and optical devices. E.C.C. and C.-H.L. acquired and analyzed the presented ADF-STEM data, while A.R. and Y.-T.S. performed early STEM explorations under the supervision of D.A.M. Z.H., Z.T., and Z.X. performed the optical measurements. Z.H., W.Z., Z.X., and J.L. performed the SHG measurements. Z.H., Y.X., and Yichi Zhang performed the transport measurements. B.S., T.L., S.J., and Yihang Zeng performed early experiments under the supervision of K.F.M. and J.S. K.W. and T.T. grew the bulk hBN crystals. K.F.M. and J.S. designed the scientific objectives and oversaw the project. All authors discussed the results and commented on the paper.

Funding

Open access funding provided by Max Planck Society.

Notes

The authors declare no competing financial interest.

■ ACKNOWLEDGMENTS

This work was supported by the Gordon and Betty Moore Foundation (Grant DOI 10.37807/GBMF11563; transport measurements) and the Air Force Office of Scientific Research under Award Number FA9550-20-1-0219 (optical measurements). E.C.C. is supported by the Air Force Office of Scientific Research under award number FA9550-23-1-0688. C.-H.L. acknowledges the support by the Eric and Wendy Schmidt AI in Science Postdoctoral Fellowship, a program of Schmidt Sciences, LLC. Sample fabrication was carried out at the Cornell NanoScale Facility, an NNCI member supported by NSF Grant NNCI-2025233. This work also used facilities of the Platform for the Accelerated Realization, Analysis, and Discovery of Interface Materials (PARADIM) and Cornell

Center for Materials Research (CCMR) supported by NSF DMR-2039380 and DMR-1719875. The growth of the hBN crystals was supported by the Elemental Strategy Initiative of MEXT, Japan, and CREST (JPMJCR15F3), JST.

REFERENCES

(1) Li, T.; et al. Continuous Mott transition in semiconductor moiré superlattices. *Nature* **2021**, *597*, 350−354.
(2) Hu, N. C.; MacDonald, A. H. Competing magnetic states in transition metal dichalcogenide moiré materials. *Phys. Rev. B* **2021**, *104*, No. 214403.
(3) Morales-Durán, N.; MacDonald, A. H.; Potasz, P. Metal-insulator transition in transition metal dichalcogenide heterobilayer moiré superlattices. *Phys. Rev. B* **2021**, *103*, No. L241110.
(4) Matty, M.; Kim, E.-A. Melting of generalized Wigner crystals in transition metal dichalcogenide heterobilayer Moiré systems. *Nat. Commun.* **2022**, *13*, 7098.
(5) Musser, S.; Senthil, T.; Chowdhury, D. Theory of a continuous bandwidth-tuned Wigner-Mott transition. *Phys. Rev. B* **2022**, *106*, No. 155145.
(6) Musser, S.; Senthil, T. Metal to Wigner-Mott insulator transition in two-leg ladders. *Phys. Rev. B* **2022**, *106*, No. 235148.
(7) Pan, H.; Das Sarma, S. Interaction range and temperature dependence of symmetry breaking in strongly correlated two-dimensional moiré transition metal dichalcogenide bilayers. *Phys. Rev. B* **2022**, *105*, No. 041109.
(8) Kim, S.; Senthil, T.; Chowdhury, D. Continuous Mott transition in moiré semiconductors: role of long-wavelength inhomogeneities. *Phys. Rev. Lett.* **2023**, *130*, No. 066301.
(9) Kiely, T. G.; Chowdhury, D. Continuous Wigner-Mott transitions at $\nu = 1/5$. *Phys. Rev. B* **2024**, *110*, No. L241112.
(10) Tan, Y.; Tsang, P. K. H.; Dobrosavljević, V. Disorder-dominated quantum criticality in moiré bilayers. *Nat. Commun.* **2022**, *13*, 7469.
(11) Xu, Y.; et al. Interaction-driven metal-insulator transition with charge fractionalization. *Physical Review X* **2022**, *12*, No. 021067.
(12) Zhou, Y.; Sheng, D.; Kim, E.-A. Quantum phases of transition metal dichalcogenide moiré systems. *Phys. Rev. Lett.* **2022**, *128*, No. 157602.
(13) Xie, M.; Pan, H.; Wu, F.; Das Sarma, S. Nematic excitonic insulator in transition metal dichalcogenide moiré heterobilayers. *Phys. Rev. Lett.* **2023**, *131*, No. 046402.
(14) Zhou, Y.; Sheng, D.; Kim, E.-A. Quantum melting of generalized Wigner crystals in transition metal dichalcogenide moiré systems. *Phys. Rev. Lett.* **2024**, *133*, No. 156501.
(15) Tao, Z.; et al. Observation of spin polarons in a frustrated moiré Hubbard system. *Nat. Phys.* **2024**, *20*, 783−787.
(16) Bohrdt, A.; Homeier, L.; Reinmoser, C.; Demler, E.; Grusdt, F. Exploration of doped quantum magnets with ultracold atoms. *Annals of Physics* **2021**, *435*, No. 168651.
(17) Ciorciaro, L.; et al. Kinetic magnetism in triangular moiré materials. *Nature* **2023**, *623*, 509−513.
(18) Davydova, M.; Zhang, Y.; Fu, L. Itinerant spin polaron and metallic ferromagnetism in semiconductor moiré superlattices. *Phys. Rev. B* **2023**, *107*, No. 224420.
(19) Seifert, U. F.; Balents, L. Spin polarons and ferromagnetism in doped dilute moiré-Mott insulators. *Phys. Rev. Lett.* **2024**, *132*, No. 046501.
(20) Zhao, W.; et al. Gate-tunable heavy fermions in a moiré Kondo lattice. *Nature* **2023**, *616*, 61−65.
(21) Zhao, W.; et al. Emergence of ferromagnetism at the onset of moiré Kondo breakdown. *Nat. Phys.* **2024**, *20*, 1772−1777.
(22) Han, Z.; et al. Topological Kondo insulator in $MoTe_2/WSe_2$ moiré bilayers. *Nat. Phys.* **2026**, *22*, 396−401.
(23) Kumar, A.; Hu, N. C.; MacDonald, A. H.; Potter, A. C. Gate-tunable heavy fermion quantum criticality in a moiré Kondo lattice. *Phys. Rev. B* **2022**, *106*, No. L041116.
(24) Guerci, D.; Wang, J.; Zang, J.; Cano, J.; Pixley, J. H.; Millis, A. Chiral Kondo lattice in doped $MoTe_2/WSe_2$ bilayers. *Science Advances* **2023**, *9*, No. eade7701.
(25) Guerci, D.; et al. Topological Kondo semimetal and insulator in AB-stacked heterobilayer transition metal dichalcogenides. *Phys. Rev. B* **2024**, *110*, No. 165128.
(26) Mendez-Valderrama, J. F.; Kim, S.; Chowdhury, D. Correlated topological mixed-valence insulators in moiré heterobilayers. *Phys. Rev. B* **2024**, *110*, No. L201105.
(27) Xie, F.; Chen, L.; Si, Q. Kondo effect and its destruction in heterobilayer transition metal dichalcogenides. *Physical Review Research* **2024**, *6*, No. 013219.
(28) Xie, F.; Chen, L.; Fang, Y.; Si, Q. Topological Kondo semimetals emulated in heterobilayer transition metal dichalcogenides. *Physical Review Research* **2025**, *7*, No. 033093.
(29) Li, T.; et al. Quantum anomalous Hall effect from intertwined moiré bands. *Nature* **2021**, *600*, 641−646.
(30) Tschirhart, C.; et al. Intrinsic spin Hall torque in a moiré Chern magnet. *Nat. Phys.* **2023**, *19*, 807−813.
(31) Zhang, Y.; Devakul, T.; Fu, L. Spin-textured Chern bands in AB-stacked transition metal dichalcogenide bilayers. *Proc. Natl. Acad. Sci. U. S. A.* **2021**, *118*, No. e2112673118.
(32) Chang, Y.-W.; Chang, Y.-C. Quantum anomalous Hall effect and electric-field-induced topological phase transition in AB-stacked $MoTe_2/WSe_2$ moiré heterobilayers. *Phys. Rev. B* **2022**, *106*, No. 245412.
(33) Devakul, T.; Fu, L. Quantum anomalous Hall effect from inverted charge transfer gap. *Physical Review X* **2022**, *12*, No. 021031.
(34) Pan, H.; Xie, M.; Wu, F.; Das Sarma, S. Topological phases in AB-stacked $MoTe_2/WSe_2$: Z_2 topological insulators, Chern insulators, and topological charge density waves. *Phys. Rev. Lett.* **2022**, *129*, No. 056804.
(35) Xie, Y.-M.; Zhang, C.-P.; Hu, J.-X.; Mak, K. F.; Law, K. Valley-polarized quantum anomalous Hall state in moiré $MoTe_2/WSe_2$ heterobilayers. *Phys. Rev. Lett.* **2022**, *128*, No. 026402.
(36) Mai, P.; Zhao, J.; Feldman, B. E.; Phillips, P. W. 1/4 is the new 1/2 when topology is intertwined with Mottness. *Nat. Commun.* **2023**, *14*, 5999.
(37) Zhao, W.; et al. Realization of the Haldane Chern insulator in a moiré lattice. *Nat. Phys.* **2024**, *20*, 275−280.
(38) Luo, X.-J.; Wang, M.; Wu, F. Symmetric Wannier states and tight-binding model for quantum spin Hall bands in AB-stacked $MoTe_2/WSe_2$. *Phys. Rev. B* **2023**, *107*, No. 235127.
(39) Andrei, E. Y.; et al. The marvels of moiré materials. *Nature Reviews Materials* **2021**, *6*, 201−206.
(40) Kennes, D. M.; et al. Moiré heterostructures as a condensed-matter quantum simulator. *Nat. Phys.* **2021**, *17*, 155−163.
(41) Mak, K. F.; Shan, J. Semiconductor moiré materials. *Nat. Nanotechnol.* **2022**, *17*, 686−695.
(42) Nuckolls, K. P.; Yazdani, A. A microscopic perspective on moiré materials. *Nature Reviews Materials* **2024**, *9*, 460−480.
(43) Xiao, D.; Liu, G.-B.; Feng, W.; Xu, X.; Yao, W. Coupled spin and valley physics in monolayers of MoS_2 and other group-VI dichalcogenides. *Physical Review Letters* **2012**, *108*, No. 196802.
(44) Tang, Y.; et al. Simulation of Hubbard model physics in WSe_2/WS_2 moiré superlattices. *Nature* **2020**, *579*, 353−358.
(45) Regan, E. C.; et al. Mott and generalized Wigner crystal states in WSe_2/WS_2 moiré superlattices. *Nature* **2020**, *579*, 359−363.
(46) Li, Y.; et al. Probing symmetry properties of few-layer MoS_2 and h-BN by optical second-harmonic generation. *Nano Lett.* **2013**, *13*, 3329−3333.
(47) Malard, L. M.; Alencar, T. V.; Barboza, A. P. M.; Mak, K. F.; De Paula, A. M. Observation of intense second harmonic generation from MoS_2 atomic crystals. *Phys. Rev. B* **2013**, *87*, No. 201401.
(48) Kumar, N.; et al. Second harmonic microscopy of monolayer MoS_2. *Phys. Rev. B* **2013**, *87*, No. 161403.
(49) Krivanek, O. L.; et al. Atom-by-atom structural and chemical analysis by annular dark-field electron microscopy. *Nature* **2010**, *464*, 571−574.

https://doi.org/10.1021/acs.nanolett.6c02425
Nano Lett. 2026, 26, 14829−14836

(50) Wang, Y.et al. Destructive interference of second harmonic generation in AA stacked $MoTe_2/WSe_2$. arXiv, arXiv:2605.21231, 2026 (accessed 2026-10-15).
(51) Zhao, W.et al. Emergence of Chern metal in a moiré Kondo lattice. arXiv, arXiv:2506.14063, 2025 (accessed 2026-10-15).
(52) Wu, F.; Lovorn, T.; Tutuc, E.; Martin, I.; MacDonald, A. Topological insulators in twisted transition metal dichalcogenide homobilayers. *Physical Review Letters* **2019**, *122*, No. 086402.
(53) Devakul, T.; Crépel, V.; Zhang, Y.; Fu, L. Magic in twisted transition metal dichalcogenide bilayers. *Nat. Commun.* **2021**, *12*, 6730.
(54) Tao, Z.; et al. Valley-coherent quantum anomalous Hall state in AB-stacked $MoTe_2/WSe_2$ bilayers. *Physical Review X* **2024**, *14*, No. 011004.
(55) Wang, L.; et al. Correlated electronic phases in twisted bilayer transition metal dichalcogenides. *Nature materials* **2020**, *19*, 861−866.
(56) Bi, Z.; Fu, L. Excitonic density wave and spin-valley superfluid in bilayer transition metal dichalcogenide. *Nat. Commun.* **2021**, *12*, 642.
(57) Zang, J.; Wang, J.; Cano, J.; Georges, A.; Millis, A. Dynamical mean-field theory of moiré bilayer transition metal dichalcogenides: Phase diagram, resistivity, and quantum criticality. *Physical Review X* **2022**, *12*, No. 021064.
(58) Cai, J.; et al. Signatures of fractional quantum anomalous Hall states in twisted $MoTe_2$. *Nature* **2023**, *622*, 63−68.
(59) Zeng, Y.; et al. Thermodynamic evidence of fractional Chern insulator in moiré $MoTe_2$. *Nature* **2023**, *622*, 69−73.
(60) Park, H.; et al. Observation of fractionally quantized anomalous Hall effect. *Nature* **2023**, *622*, 74−79.
(61) Xu, F.; et al. Observation of integer and fractional quantum anomalous Hall effects in twisted bilayer $MoTe_2$. *Physical Review X* **2023**, *13*, No. 031037.
(62) Xia, Y.; et al. Superconductivity in twisted bilayer WSe_2. *Nature* **2025**, *637*, 833−838.
(63) Guo, Y.; et al. Superconductivity in 5.0° twisted bilayer WSe_2. *Nature* **2025**, *637*, 839−845.
(64) Han, Z.et al. Quantum oscillations between excitonic and quantum spin Hall insulators in moiré WSe_2. *arXiv*, 2025, arXiv:2509.19287 (accessed 2026-10-15).
(65) Xia, Y.; Han, Z.; Zhu, J.; Zhang, Y.; Knuppel, P.; Watanabe, K.; Taniguchi, T.; Mak, K. F.; Shan, J. Bandwidth-tuned Mott transition and superconductivity in moiré WSe_2. *Nature* **2026**, *650*, 585−591.
(66) Guo, Y.; et al. Angle evolution of the superconducting phase diagram in twisted bilayer WSe_2. *Nature* **2026**, *652*, 622−627.
(67) Zhang, Y.-H. Doping a Mott insulator with excitons in a moiré bilayer: fractional superfluid, neutral Fermi surface, and Mott transition. *Phys. Rev. B* **2022**, *106*, No. 195120.
(68) Chang, X.; Tao, Z.; Shen, B.; Tian, W.; Hu, J.; Pistunova, K.; Watanabe, K.; Taniguchi, T.; Heinz, T. F.; Li, T.; Mak, K. F.; Shan, J.; Jiang, S. Electric-Field-Tuned Consecutive Topological Phase Transitions between Distinct Correlated Insulators in Moiré $MoTe_2/WSe_2$ Heterobilayer. *Phys. Rev. Lett.* **2026**, *136*, No. 096503.

https://doi.org/10.1021/acs.nanolett.6c02425
Nano Lett. 2026, 26, 14829−14836